JOURNAL OF APPLIED ELECTROCHEMISTRY 26 (1996) 1147–1160

Electrochemistry of room-temperature chloroaluminate molten salts at graphitic and nongraphitic electrodes

R. T. CARLIN,*‡ J. FULLER, W. K. KUHN, M. J. LYSAGHT, P. C. TRULOVE

The Frank J. Seiler Research Laboratory, 2354 Vandenberg Drive, Suite 2A35, United States Air Force Academy, Colorado 80840-6272, USA

Received 17 July 1995; revised 18 January 1996

The electrochemistry of unbuffered and buffered neutral $AlCl_3$–EMIC–MCl (EMIC = 1-ethyl-3-methylimidazolium chloride and MCl = LiCl, NaCl or KCl) room-temperature molten salts was studied at graphitic and nongraphitic electrodes. In the case of the unbuffered 1 : 1 $AlCl_3$: EMIC molten salt, the organic cation reductive intercalation at about −1.6 V and the $AlCl_4^-$ anion oxidative intercalation at about +1.8 V were evaluated at porous graphite electrodes. It was determined that the instability of the organic cation in the graphite lattice limits the performance of a dual intercalating molten electrolyte (DIME) cell based on this electrolyte. In buffered neutral 1.1 : 1.0 : 0.1 $AlCl_3$: EMIC : MCl (MCl = LiCl, NaCl and KCl) molten salts, the organic cation was intercalated into porous and nonporous graphite electrodes with similar cycling efficiencies as the unbuffered 1 : 1 melt; however, additional nonintercalating processes were also found to occur between −1 and −1.6 V in the LiCl and NaCl systems. A black electrodeposit, formed at −1.4 V in the LiCl buffered neutral melt, was analysed with X-ray photoelectron spectroscopy and X-ray diffraction and was found to be composed of LiCl, metallic phases containing lithium and aluminium, and an alumina phase formed from reaction with the atmosphere. A similar film appears to form in the NaCl buffered neutral melt, but at a much slower rate. These films are believed to form by reduction of the $AlCl_4^-$ anion, a process promoted by decreasing the ionic radius of the alkali metal cation in the molten salt. The partially insulating films may limit the usefulness of the LiCl and NaCl buffered neutral melts as electrolytes for rechargeable graphite intercalation anodes and may interfere with other electrochemical processes occurring negative of −1 V.

1. Introduction

We have recently described the concept of dual intercalating molten electrolyte (DIME) batteries in which the anion and the cation of a low-temperature molten salt electrolyte are both intercalated into graphite electrodes [1]. The reversible reductive intercalation of the cation constitutes a rechargeable anode, while the reversible oxidative intercalation of the anion provides a rechargeable cathode. The DIME cell configuration offers several practical advantages: (i) inexpensive graphite electrodes are used for both the anode and cathode; (ii) only a single molten salt needs to be synthesized and purified; (iii) no organic solvents are required; and (iv) the cell can be assembled in the discharged state.

The room-temperature molten salt formed from the combination of 1-ethyl-3-methylimidazolium chloride (EMIC) and aluminium chloride is perhaps the most studied of the known room-temperature melts for a wide variety of applications, including batteries, metal electrodeposition, organic reactions, catalysis, and inorganic cluster chemistry [2, 3]. Initial studies of 1 : 1 $AlCl_3$: EMIC as a DIME battery electrolyte indicated that EMI^+ was not fully stable in the graphite lattice; however, only a cursory investigation was performed [1]. Because of the wide interest in the $AlCl_3$–EMIC molten salt, we have extended our graphite intercalation studies of this melt and report the results here.

In this paper, we will also discuss our recent investigations of buffered neutral $AlCl_3$–EMIC–MCl (MCl = LiCl, NaCl and KCl) melts [4] as DIME battery electrolytes. In these buffered neutral melts, excess $Al_2Cl_7^-$ is converted to $AlCl_4^-$ by reaction with solid MCl, and free chloride ions are precipitated as MCl; therefore, the only anion present is $AlCl_4^-$. This is an essential requirement for the chloroaluminate DIME battery configuration because $Al_2Cl_7^-$ is reduced positive of the organic cation reductive intercalation, and Cl^- is oxidized negative of the $AlCl_4^-$ oxidative intercalation. However, for NaCl buffered melts, an apparent lack of complete buffering, giving a slightly acidic melt (excess $Al_2Cl_7^-$), has been reported [5]. Additionally, a 'latent acidity' has been reported for NaCl buffered neutral melts in which

* To whom correspondence should be addressed.
‡ Present address: Covalent Associates, Inc., 10 State Street, Woburn, MA 01801, USA.

0021-891X

$AlCl_4^-$ reacts with relatively weak bases to form $AlCl_3$ complexes, the driving force of the reaction being precipitation of NaCl [6]. Any incomplete buffering towards an acidic composition may lead to the electrodeposition of aluminium or aluminium alloys on the graphite electrode surface, hindering the cation reductive intercalation process. For example, Fung and Chau reported the electrodeposition of lithium–aluminium alloys in LiCl buffered neutral melts [7]. Therefore, we have examined the reductive intercalation process at graphite in LiCl, NaCl, and KCl buffered neutral melts and have identified other nonintercalation reduction processes occurring at the electrode surface prior to the reductive intercalation.

2. Experimental details

$EMIAlCl_4$ and $AlCl_3$–EMIC–MCl melts (MCl = LiCl, NaCl and KCl) were prepared as previously described [1, 4]. All buffered neutral melt were prepared with $AlCl_3$: EMIC : MCl molar ratios of 1.1 : 1.0 : 0.1, giving alkali metal ion concentrations of approximately 0.45 M [4]. Voltammetric experiments were performed using an EG&G PARC (model 273) potentiostat/galvanostat controlled with the EG&G PARC 270 software package. All experiments were performed in a vacuum atmosphere glove box under helium with an $O_2 + H_2O$ concentration of <5 ppm.

To achieve complete buffering, melts were stirred for several days prior to use. Excess solid MCl was left in the buffered melt to ensure that the buffered state was maintained for the entire experimental time, often several weeks. Although some concerns are often raised regarding the possibility that melts are not fully buffered [5], we believe our procedures provide melts that are as close to buffered neutral as is thermodynamically possible.

The graphite rod working electrode was a high purity, spectroscopic grade graphite rod with a 3 mm diameter (Union Carbide), pretreated by drying at 400 °C for several hours in air and cooling under vacuum in the glove box antechamber. The graphite sheet working electrode was a 1/4 inch wide strip cut from a 0.254 inch thick graphite sheet having a purity of 99.9% (Johnson Matthey); it was pretreated in the same manner as the graphite rod electrode. The graphite electrodes were immersed in the molten salt electrolyte, and the geometric area wetted by the electrolyte was measured and used to convert currents to current densities. The geometric area was generally about 1 cm^2; however, these areas do not take into account the porosity and roughness of the electrodes.

The nickel foil electrodes were cut from a 0.15 mm thick foil as strips (~0.5 cm × 1 cm) or as flag electrodes (~2 cm × 2 cm). The nickel foil surface was polished with 1.0 and 0.25 μm alumina, rinsed with ethanol, and dried at about 100 °C. Geometric areas immersed in the molten salts ranged from 2 to 9 cm^2.

The glassy carbon (GC, 3 mm diam.) disc electrode was purchased from Bioanalytical Systems. The reference electrode consisted of an aluminium wire immersed in a 1.5 : 1.0 $AlCl_3$: EMIC melt contained in a separate fritted glass tube. The counter electrode was an aluminium wire dipped into a portion of the analyte melt contained in a 3 mm o.d., D-porosity gas dispersion tube (Ace Glass).

X-ray diffraction (XRD) measurements were made with a Rigaku DMAX/B diffractometer fitted with parallel optics for thin film analysis. Samples for XRD analysis were protected from the air by sealing them between two pieces of tape before removal from the glove box; samples properly sealed in this manner were stable for >10 h. Thin film diffraction patterns were collected in the 2θ scan mode (scan rate 2 ° min^{-1}) using CuK_α (λ = 154.060 pm) with the sample surface at 3 ° to the incident X-ray beam. To increase signal-to-noise ratios, final diffraction patterns were the sum of 3 to 5 independent scans; this allowed easy identification of all phases and helped to confirm the lack of any diffraction lines which could be assigned to Li–Al alloy phases.

The X-ray photoelectron spectroscopy (XPS) analyses were performed with a Perkin–Elmer Physical Electronics 5600ci ESCA instrument, equipped with a Mg/Al dual anode X-ray source, a 5 kV differentially pumped ion gun, and a hemispherical electron energy analyser. The system had a base pressure of $\leqslant 2 \times 10^{-10}$ torr (2.7×10^{-8} Pa) with a typical operating pressure of 7×10^{-10} torr (9.3×10^{-8} Pa) during data acquisition. The XPS spectra were acquired using an AlK_α X-ray source operating at 400 W. Sputter cleaning of the samples was performed using Ar^+ ions with a kinetic energy of 3.5 keV and a beam current of 2.5 μA. For the sputter cleaning, the ion beam was rastered over a 2 mm × 2 mm area of the sample with a 40 ° angle of incidence relative to the sample surface normal. The analysis area on the sample was 800 μm in diameter, and photoelectron detection was taken at 45 ° off the surface normal. Peak binding energies were corrected for charging by shifting the energy scale such that the carbon 1 *s* peak had a binding energy of 284.8 eV. This procedure gave an experimental uncertainty in the measured binding energies of ±0.1 eV.

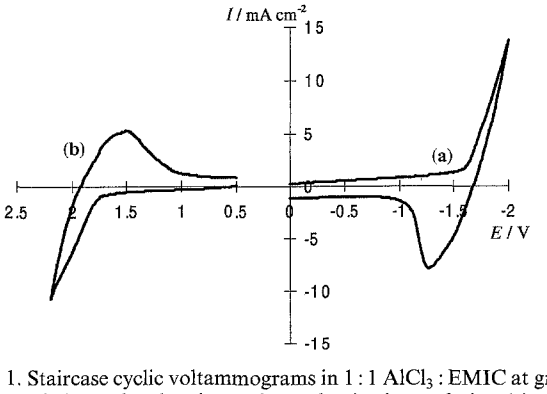

Fig. 1. Staircase cyclic voltammograms in 1 : 1 $AlCl_3$: EMIC at graphite rod electrodes showing cation reductive intercalation (a) and anion oxidative intercalation (b). Scan rate 25 mV s^{-1}.

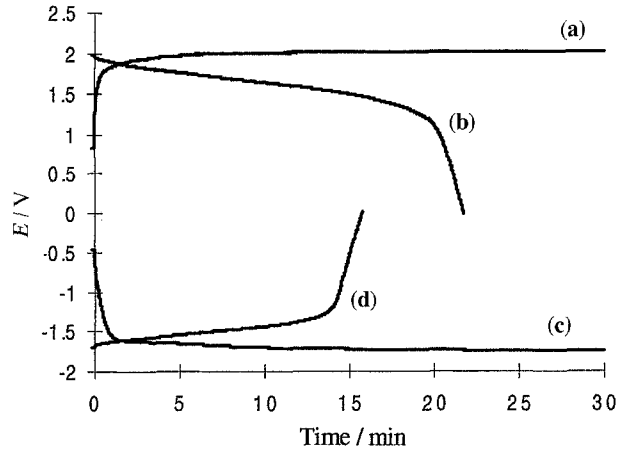

Fig. 2. Chronopotentiometry for anion intercalation (a) and deintercalation (b) and cation intercalation (c) and deintercalation (d) in 1 : 1 $AlCl_3$: EMIC at a graphite rod electrode. Current density 1 mA cm^{-2}.

3. Results

3.1. *Organic cation and tetrachloroaluminate intercalation into porous graphite*

Staircase cyclic voltammograms collected in the 1 : 1 $AlCl_3$: EMIC molten salt electrolyte show EMI^+ intercalation–deintercalation at −1.6 V (Fig. 1(a)) and $AlCl_4^-$ intercalation–deintercalation at +1.8 V (Fig. 1(b)) with cycling efficiencies of 66 and 85%, respectively. The graphite intercalation processes occur well within the electrochemical limits of the melt which, at a nonintercalating GC electrode, are found at −2.2 V and +2.5 V, corresponding to EMI^+ reduction and $AlCl_4^-$ oxidation, respectively [1].

Representative chronopotentiometric curves for cation and anion intercalation–deintercalation are shown in Fig. 2. The relevant parameters for EMI^+ and $AlCl_4^-$ intercalation studied with chronopotentiometry are presented in Table 1. Cycling efficiencies were calculated as % efficiency = 100 × (intercalation time ÷ deintercalation time). The cycling efficiency for $AlCl_4^-$ is relatively high, about 80%; however, the EMI^+ cycling efficiency is poor in all cases. The poor performance of the EMI^+ electrode is further magnified by the rapid loss in efficiency when a time delay at open circuit is imposed between the charge and discharge steps. This instability of EMI^+ may involve reaction of the relatively acidic C-2 proton [8] with the negatively charged graphite lattice. This is supported by the high cycling efficiencies observed for the reductive intercalation of the 1,2-dimethyl-3-propylimidazolium cation ($DMPI^+$) in which the C-2 proton has been replaced by a methyl group [1].

A DIME battery cell was constructed by inserting two graphite rod electrodes into the 1 : 1 $AlCl_3$: EMIC melt. The cell performance is summarized in Table 2. Based on a comparison of cycling efficiencies in Tables 1 and 2, it appears that the instability of EMI^+ limits the performance of this DIME cell configuration. Better DIME cell performance is obtained with the $AlCl_3$–DMPIC molten salt electrolyte [1].

3.2. *Reduction processes at graphitic and GC electrodes in buffered neutral $AlCl_3$–EMIC–MCl electrolytes*

As discussed earlier, the DIME battery configuration requires that the $AlCl_3$–EMIC molten salt have an exactly neutral composition, that is, the $AlCl_3$: EMIC molar ratio must be exactly one. However, it is often difficult to achieve and maintain this exact 1 : 1 stoichiometry. To try to alleviate this difficulty, we have employed buffered neutral melts as electrolytes for the intercalation electrodes.

The cation intercalation-deintercalation processes at a graphite rod electrode in 1.1 : 1.0 : 0.1 $AlCl_3$: EMIC : MCl, where MCl = LiCl, NaCl and KCl, are illustrated by the staircase cyclic voltammograms shown in Fig. 3. In all three systems, the reductive intercalation occurs at about −1.6 V, while the deintercalation is a broad peak at about −1.4 V. For the LiCl and NaCl buffered neutral melts, additional cathodic and anodic processes are seen and are discussed in more detail below. From integration of the cathodic and anodic currents negative of −0.6 V, the cycling efficiencies are calculated to be 65, 54 and 63% for the LiCl, NaCl and KCl buffered neutral melts, respectively. These efficiencies are comparable to the results found for the exactly 1 : 1 EMIC : $AlCl_3$ melt in Table 1 and are consistent with the intercalation-deintercalation of the organic cation.

It is highly desirable to have the organic cation undergoing the intercalation in these molten salt electrolytes because the concentration of the organic

Table 1. Chronopotentiometric studies of EMI^+ and $AlCl_4^-$ intercalation into graphite using 1 : 1 $AlCl_3$: EMICl
All runs conducted at 31 °C with a charging time of 30 min.

Intercalating ion	I_{charge} /mA cm^{-2}	E_{charge} /V	$I_{discharge}$ /mA cm^{-2}	$E_{discharge}$ /V	*Time delay*	*Efficiency* /%
$AlCl_4^-$	1	+2.01	1	+1.64	N/A	68
$AlCl_4^-$	1	+1.97	0.5	+1.64	N/A	79
$AlCl_4^-$	1	+1.95	0.25	+1.65	N/A	79
EMI^+	1	−1.72	1	−1.49	N/A	48
EMI^+	1	−1.72	0.5	−1.51	N/A	49
EMI^+	1	−1.73	0.25	−1.52	N/A	57
EMI^+	1	−1.73	0.25	−1.51	30 min	51
EMI^+	1	−1.73	0.25	−1.44	4 h	29
EMI^+	1	−1.73	0.25	−1.27	10.5 h	2

Table 2. Performance parameters for a dual intercalating molten electrolyte (DIME) battery cell
All runs conducted at 31 °C with a charging time of 30 min.

E_{open} /V	I_{charge} /mA cm^{-2}	E_{charge} /V	$I_{discharge}$ /mA cm^{-2}	$E_{discharge}$ /V	*Time delay*	*Efficiency* /%
−3.14	1	−3.69	1	−3.15	N/A	63
−3.36	1	−3.76	0.5	−3.14	N/A	60
−3.23	1	−3.71	0.25	−3.25	N/A	61
−2.87	1	−3.70	1	−3.12	30 min	62
−2.62	1	−3.70	1	−2.80	4.3 h	27
−3.05	1	−3.71	1	−2.80	6.1 h	25
–	1	−3.70	1	−1.40	17.5 h	0

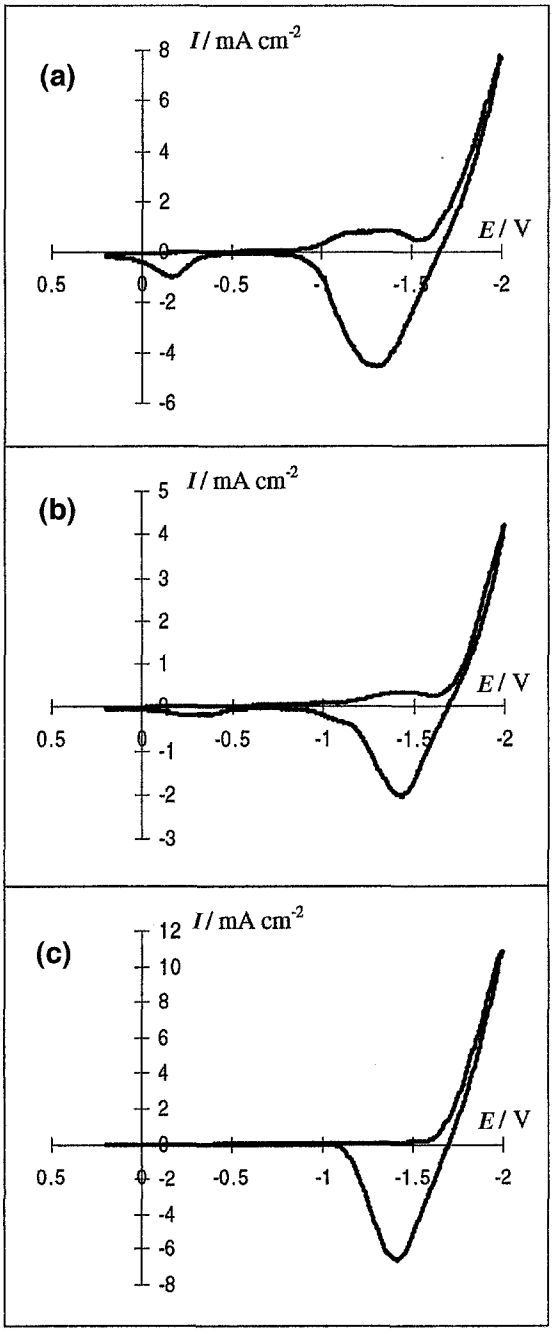

Fig. 3. Staircase cyclic voltammograms to −2.0 V showing organic cation reductive intercalation at graphite rod electrodes in 1.1 : 1.0 : 0.1 $AlCl_3$: EMIC : MCl, where MCl = LiCl (a), NaCl (b), and KCl (c). Switching potential −2.0 V; scan rate 1 mV s^{-1}. For all plots, the abscissa V vs Al/Al(III) reference, and the ordinate (current density) is mA cm^{-2}.

cation in a 1.1 : 1.0 : 0.1 $AlCl_3$–EMIC–KCl electrolyte is about 4.0 M, while the concentration of M^+ is only about 0.45 M. If only M^+ underwent intercalation–deintercalation in the buffered neutral melts, then the charge-to-weight ratio of the cell would be quite low. For a 1 : 1 $AlCl_3$: EMIC DIME cell, the theoretical energy density is 95 Wh kg^{-1}, based on fully charged anode and cathode compositions of (EMI) C_{24} and $(AlCl_4)C_{24}$, respectively. These electrode compositions are postulated stoichiometries and are based on previous results for large anion and quaternary ammonium graphite intercalates [9, 10]. We have not yet experimentally determined the composition of charged DIME electrodes.

It is apparent from the voltammograms for the LiCl and NaCl buffered neutral melts (Fig. 3(a) and 3(b)) that additional reduction processes are occurring at potentials positive of the reductive intercalation at −1.6 V. To study these other cathodic processes, the scan direction was reversed before the reductive intercalation; the resulting voltammograms are shown in Fig. 4 for the three buffered neutral systems. Several features of the voltammograms are important: (i) cathodic currents are highest for the LiCl buffered neutral melt (Fig. 4(a)); (ii) two anodic waves at about −1.2 and −0.3 V are seen for the LiCl and NaCl systems; and (iii) the KCl buffered neutral melt displays only low irreversible cathodic currents before a sharp rise at −1.6 V, corresponding to the onset of the EMI^+ reductive intercalation process. Integration of the cathodic and anodic currents in Fig. 4(a) for the LiCl buffered neutral melt gives a cycling efficiency of 17.3% for the first anodic wave, and a total cycling efficiency of 101.6%, when both anodic waves are included in the calculation. The total cycling efficiency of greater than 100% results from uncertainties in the voltammogram baselines. Similar integrations for the NaCl system in Fig. 4(b) give 63.9% for the first anodic wave and 100.6% for both anodic waves. No such calculations are possible for the KCl system.

We previously reported the behaviour seen in Fig. 4(a) for the LiCl buffered neutral melt and postulated a Li^+ reductive intercalation process to explain the cathodic current at −1.4 V [11]. However, assignment of the cathodic wave at −1.4 V to alkali metal ion intercalation is contradicted by the lack of a −1.4 V reduction wave in the KCl melt and the presence of a significant cathodic wave at −1.4 V for the NaCl

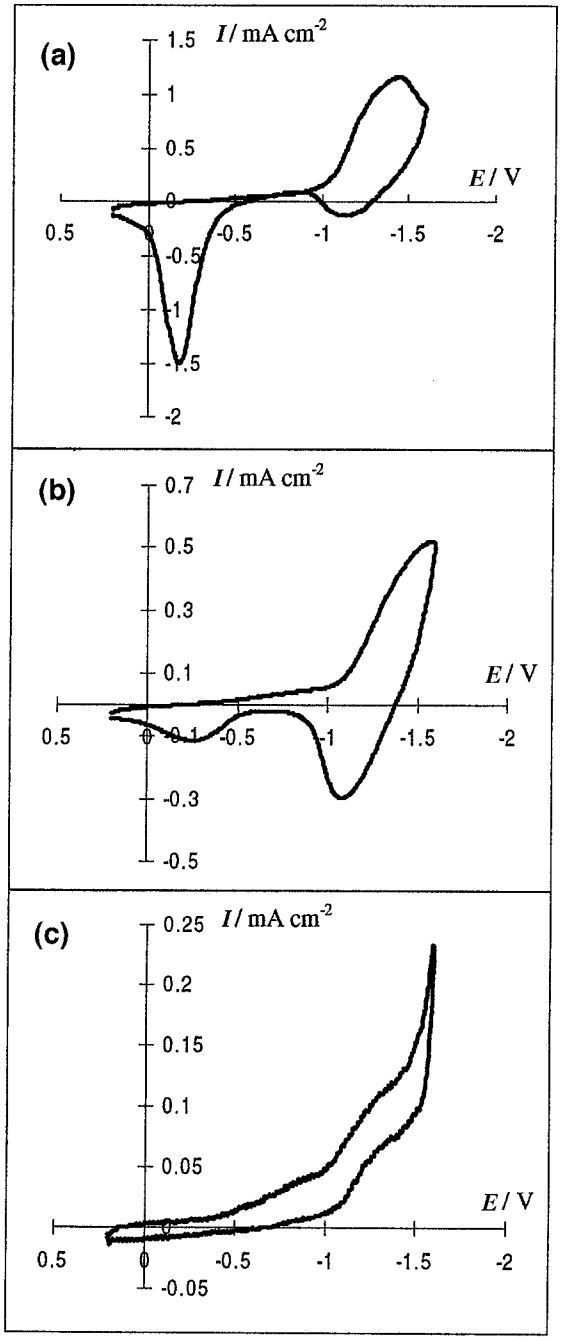

Fig. 4. Same parameters as Fig. 3, but with switching potential −1.6 V. For all plots, the abscissa is V vs Al/Al(III) reference, and the ordinate (current density) is mA cm^{-2}.

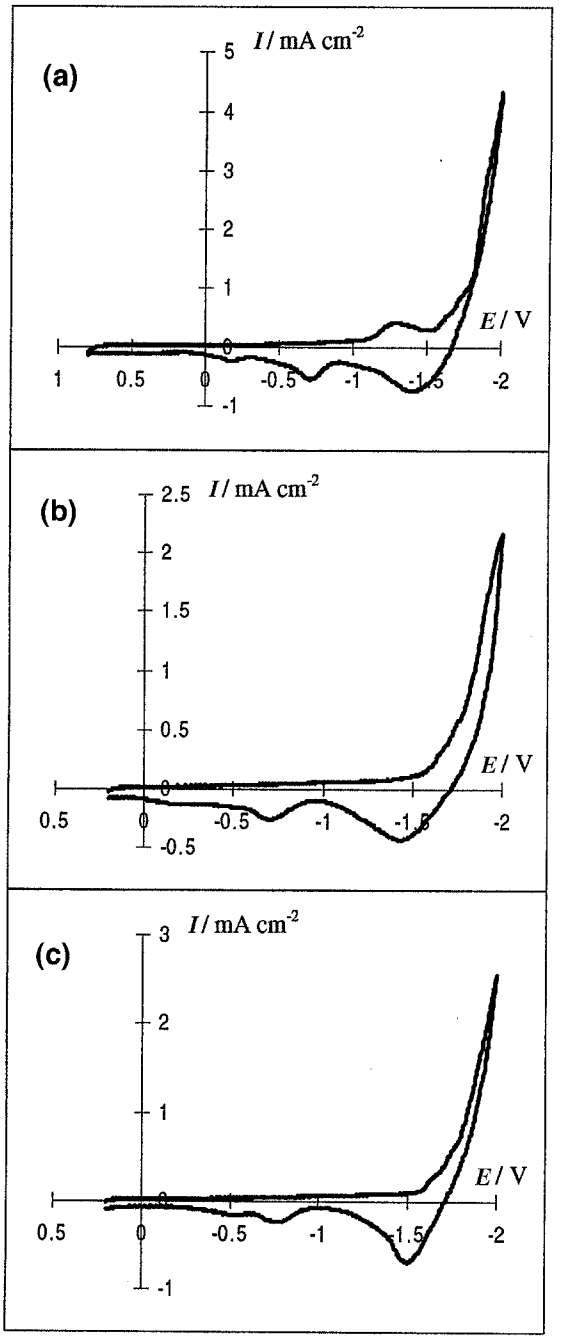

Fig. 5. Staircase cyclic voltammograms to −2.0 V showing organic cation reductive intercalation at graphite sheet electrodes in 1.1 : 1.0 : 0.1 $AlCl_3$: EMIC : MCl, where MCl = LiCl (a), NaCl (b), and KCl (c). Switching potential −2.0 V; scan rate 1 mV s^{-1}. For all plots, the abscissa is V vs Al/Al(III) reference, and the ordinate (current density) is mA cm^{-2}.

melt. It is well known that the stage one C_8K graphite intercalate is easily formed, whereas, the sodium intercalate is very difficult to form and is limited to $C_{64}Na$ [12]; $C_{15}Na$ and $C_{24}Na$ intercalates have been reported for petroleum coke electrodes [13]. Therefore, it is unlikely the process seen at −1.4 V in the NaCl system is formation of a sodium–graphite intercalate, and so it is necessary to reconsider whether the −1.4 V reduction seen in the LiCl system corresponds to formation of a lithium–graphite intercalate.

To try to answer the question of whether alkali metal intercalates are formed in the buffered neutral melts, we switched to graphite sheet electrodes which are more amenable to X-ray diffraction (XRD) studies. The graphite sheet electrodes were examined in the three buffered neutral melt systems using cyclic staircase voltammetry. Voltammograms with switching potentials of −2.0 and −1.6 V are shown in Figs 5 and 6, respectively. The reductive intercalation of the organic cation is seen at about −1.7 V in all three melts (Fig. 5); however, the organic cation deintercalation processes at −1.5 V is not as well behaved as it is for the graphite rod electrode. For scans to −1.6 V (Fig. 6), the LiCl and NaCl systems display a single anodic wave at −0.2 to −0.4 V, similar to the more positive anodic wave seen at the graphite rod electrode. The cycling efficiencies from Fig. 6 are only about 54 and 59% for the LiCl and NaCl systems, respectively. Also, the cathodic current

densities in Fig. 6 (calculated using geometric areas) are lower than those observed in Fig. 4 at a graphite rod electrode; this is likely a result of the highly porous nature of the spectroscopic grade graphite rod which has a higher electroactive surface area than the low porosity graphite sheet [12].

A graphite sheet electrode was charged at −1.4 V for 22 h in a LiCl buffered neutral melt. After this time, the surface of the graphite sheet was dull black, not the brass yellow expected for stage one C_6Li [14]. XRD thin film analysis of the top surface of the charged graphite sheet showed strong lines for crystalline LiCl, along with weak lines assigned to a Al_2O_3 perovskite phase (*vide infra*). Importantly, the diffraction lines for the graphite sheet substrate were unaltered, indicating no intercalation had occurred. No other diffraction lines were found. Using a piece of sticky tape, the dull black top surface was pulled from the graphite substrate, exposing the glossy surface of the underlying graphite sheet substrate. The dull black material decomposed rapidly when exposed to the ambient atmosphere. Therefore, based on the above information, the reduction occurring at −1.4 V in the LiCl buffered neutral melt does not correspond to lithium intercalation into graphite; instead, it is the electrodeposition of a black reactive material. A similar electrodeposit is probably formed at −1.4 V in the NaCl buffered neutral melt; however, we have not been able to produce enough of the material from the NaCl system to analyse. The chemical composition of the black electrodeposit prepared in the LiCl buffered neutral melt is discussed in more detail below.

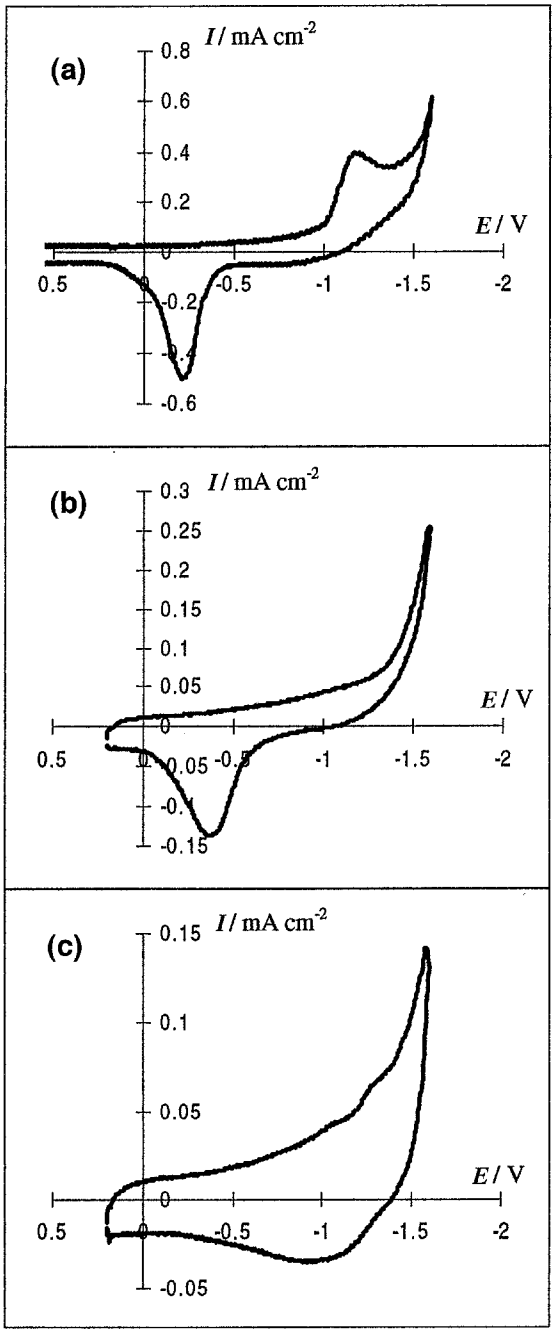

Fig. 6. Same parameters as Fig. 5, but with switching potential −1.6 V. For all plots, the abscissa is V vs Al/Al(III) reference, and the ordinate (current density) is mA cm^{-2}.

Following the above experiments with the graphite sheet electrode, the reduction process at −1.4 V in the LiCl system was studied using a nonintercalating glassy carbon electrode; the EMI^+ cation does not intercalate into GC [1]. A staircase cyclic voltammogram at GC is shown in Fig. 7 in which the potential is held at −1.4 V for 300 s before scanning in the positive direction. The anodic wave at −0.2 is essentially identical to those seen at the graphite rod and graphite sheet electrodes. A cyclic voltammogram to −1.4 V (scan rate 1 mV s^{-1}) at GC, without a potential hold, showed a small anodic wave at −0.3 V and gave a cycling efficiency of ~5%. No anodic waves were observed for cyclic voltammograms at GC in NaCl and KCl buffered neutral melts (scan rate 1 mV s^{-1}; no potential hold). Based on the above experiments, the cycling efficiency for the nonintercalating process (i.e., electrochemistry positive of −1.6 V) decreases in the order graphite rod > graphite sheet > glassy carbon. Also, only the graphite rod shows two anodic waves.

Our first thought on the nature of the black electrodeposit produced at −1.4 V in the LiCl buffered neutral melt was that it is a fine deposit of elemental Al produced by the electrochemical reaction

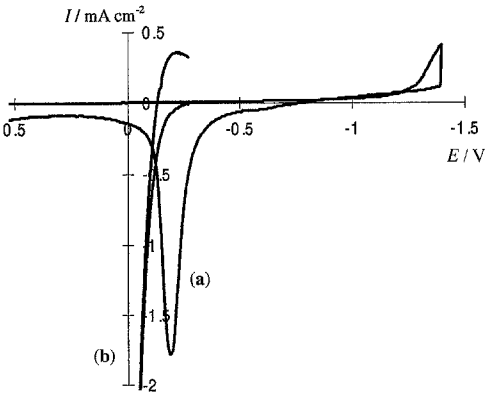

Fig. 7. Staircase cyclic voltammograms at a GC electrode (a) and an Al wire (b) in 1.1 : 1.0 : 0.1 $AlCl_3$: EMIC : LiCl. Switching potential −1.4 V with a 300 s hold; scan rate 100 mV s^{-1} (a) and 50 mV s^{-1} (b).

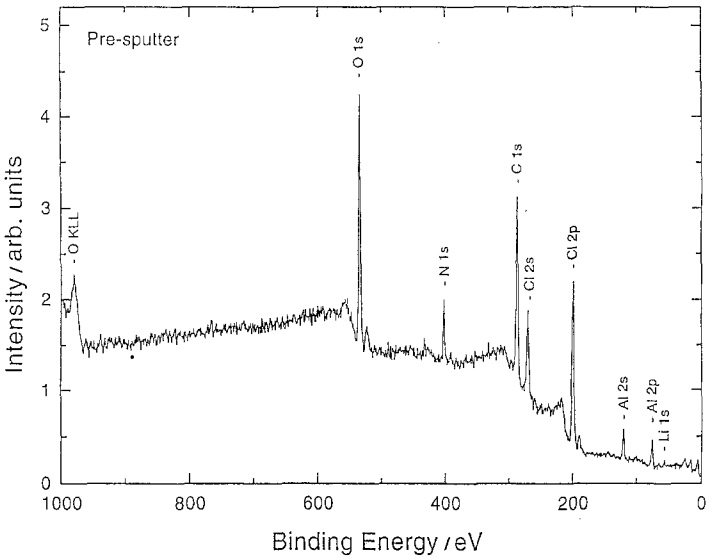

Fig. 8. Low resolution XPS spectrum of the black electrodeposit prepared on Ni foil in 1.1 : 1.0 : 0.1 $AlCl_3$: EMIC : LiCl at −1.4 V before sputtering.

$$AlCl_4^- + 3e^- + 4Li^+ \longrightarrow Al(s) + 4LiCl(s) \quad (1)$$

This would account for the presence of crystalline LiCl in the electrodeposit. Also, an extremely fine deposit of elemental Al would be black and would produce broad, possibly unobserved, diffraction lines. A similar aluminium electrodeposition has been postulated to occur in NaCl buffered neutral melts [5]; however, in this earlier report, the proposed electrodeposition of elemental Al was based solely on electrochemical observations, without additional supporting analytical methods. If the black electrodeposit is actually elemental Al, the stripping potential of the electrodeposit should be the same as an aluminium wire electrode. The anodization of an aluminium wire in a LiCl buffered neutral melt is shown in Fig. 7(b). It occurs approximately 200 mV positive of the anodization for the black electrodeposit (Fig. 7(a)) performed in the same LiCl buffered neutral melts. Therefore, the black electrodeposit is less noble than pure elemental Al.

To further demonstrate the different chemistry of the black electrodeposit, compared to pure elemental Al, electrodeposits were produced at −1.4 V in a LiCl buffered neutral melt on graphite sheet, GC, and nickel electrodes. These deposits were dipped into an acidic 1.5 : 1.0 $AlCl_3$: EMIC melt from which elemental Al is readily produced by reduction of the $Al_2Cl_7^-$ ion [2]. The black electrodeposits were converted to a grey deposit of elemental Al over several minutes. The nature of this new aluminium deposit was confirmed by XRD analysis which showed sharp diffraction lines for f.c.c. Al metal. The new elemental aluminium deposit also anodized at the same potential as an aluminium wire in the LiCl buffered neutral melt.

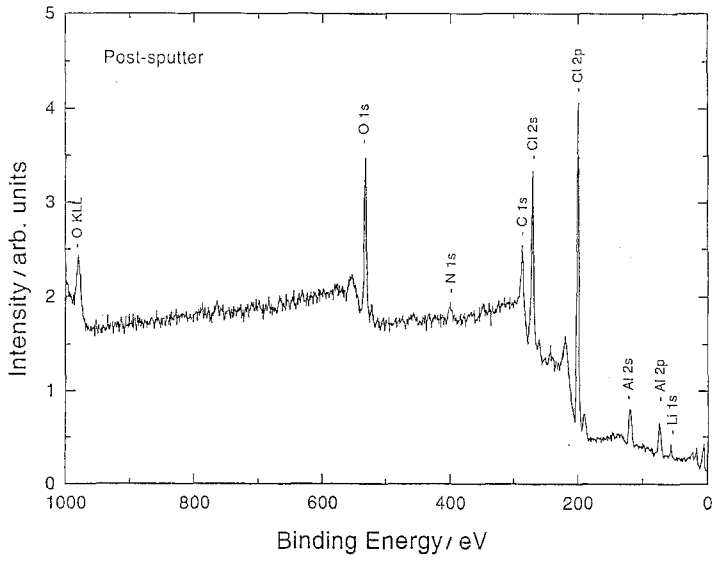

Fig. 9. Low resolution XPS spectrum of the same sample as in Fig. 8, but after 5 min of ion sputtering.

Table 3. Atomic composition of black electrodeposit prepared as determined by low resolution XPS analysis

Element	*Concentration* /at %
Li	28
Cl	27
O	19
Al	10
C	14
N	2

3.3. *XRD analysis of the black electrodeposit on Ni foil electrodes*

Several black electrodeposits were formed on nickel foil electrodes at −1.4, −1.5, and −1.6 V in the LiCl buffered neutral melt and were analyzed with a thin film XRD system. During preparation of these samples the current at constant potential was variable and sometimes erratic, often exhibiting sharp rises and falls in current, indicating a passive film breakdown followed by repassivation. Such behaviour may be attributed to formation of a partially insulating film. Because preliminary studies indicated that washing with toluene or acetonitrile degraded the samples, excess melt was only blotted from the sample surface with Kimwipes.

The XRD thin film analysis of all samples showed the presence of crystalline LiCl, substrate nickel metal, and a phase which indexed as an orthorhombic perovskite phase with $a = 5.44(2)$, $b = 7.68(3)$, $(c) = 5.47(2)$. The lattice parameters for the mineral perovskite ($CaTiO_3$) are $a = 5.4424(1)$, $b = 7.6417(2)$, $c = 5.3807(1)$ [15]. Twelve lines were used to index the perovskite phase in the black electrodeposit, all of which indexed to related diffraction lines in $CaTiO_3$. Also, there were no unassigned diffraction lines in the electrodeposit XRD pattern. At this time we can only speculate that the perovskite phase is an unidentified Al_2O_3 phase (possibly containing lithium or chloride) produced by exposure of the electrodeposit to trace oxygen in the glove box or to trace air during transfer to the XRD unit. To our knowledge, no perovskite Al_2O_3 phases have been reported to date, and most aluminas take on the spinel structure [16].

3.4. *XPS analysis of black electrodeposit on Ni foil electrodes*

XPS analyses were formed on three black electrodeposits prepared at −1.4 V on nickel foil electrodes. Deposition times ranged from 16 to 24 h. The most interesting of these samples is discussed next. Because our XPS results cannot definitively distinguish between alloyed and unalloyed metals in most cases, we use the term 'metallic' to refer to metals which may be in either an alloyed or unalloyed state, while the term 'elemental' is reserved for describing only unalloyed metals.

An XPS survey spectrum of the black electrodeposit sample, immediately after being transferred from the glove box into the UHV system, is shown in Fig. 8. This figure clearly shows that the main components on the sample surface are carbon, oxygen, chlorine, and nitrogen, indicating that the sample surface is covered with an ill-defined mixture of melt and various hydroxide species. The high hydroxide concentration is a clear reflection of the highly hygroscopic nature of these films. A light sputter (~2 min) of the sample removes much of the carbon, reduces the intensity of the oxygen peak, and increases the intensity of the aluminium, lithium, and chlorine peaks. Thus, immediately beneath the melt/hydroxide mixture on the surface, the sample appears to be a mixture of mostly aluminium oxides and lithium chloride. More prolonged sputtering (~5 min.) gives the spectrum shown in Fig. 9. In this figure, significant increases in the lithium and chlorine intensities, along with decreases in the carbon, oxygen and nitrogen intensities, are quite evident. In addition, there is a modest increase in the intensity of the aluminium peaks. Additional sputtering does not change the

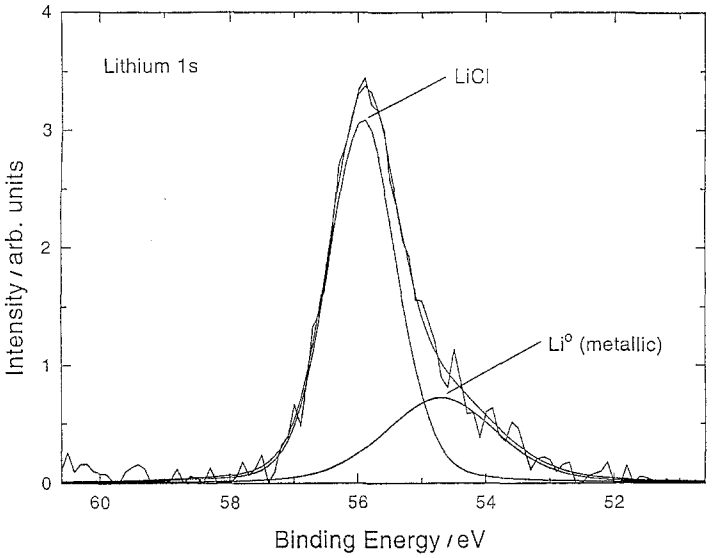

Fig. 10. High resolution XPS spectrum of Li 1*s* region for the sample shown in Fig. 9.

spectrum to any appreciable degree. Thus, the spectrum shown in Fig. 9 is representative of the bulk composition of the film.

A simple straightforward examination of the peak intensities in Fig. 9 allows determination of the atomic concentrations of the elements present; these are listed in Table 3. The results in Table 3, in conjunction with peak binding energy values, indicate that the film is primarily composed of LiCl, Al_2O_3, and some entrapped carbonaceous melt material. This is not, however, a complete picture of the film. High resolution spectra of the lithium and aluminium peaks (Figs 10 and 11, respectively) clearly show that these features are not single transitions, but are composed of multiple, overlapping peaks. In Figs 10 and 11, the experimental data, deconvoluted peaks, and composite spectrum (showing goodness of fit to experimental data) are plotted together. Both figures show that in addition to the main peak, low binding energy peaks are needed to get a precise fit to the experimental data.

Figure 10 shows the high resolution spectrum for the Li 1*s* region. It is evident from the experimental data shown in this figure that the major peak intensity occurs at 55.9 eV. The Li 1*s* binding energy for LiCl is known to be 56.0 ± 0.2 eV [17–19], and no other common lithium compounds have a binding energy closer than 0.3 eV to this value [17, 19]; therefore, this feature is unambiguously assigned to LiCl. The low binding energy shoulder, on the other hand, is more difficult to characterize. This feature can be fit either with one broad peak at 54.7 eV (as shown in Fig. 10) or with two narrow peaks at 55.0 and 53.9 eV. The generally accepted binding energies for Li, Li_2O, LiOH, and Li_2CO_3 fall between 55.6 and 54.5 eV, with elemental Li having the lowest binding energy at 54.7 ± 0.2 eV [17–20]. Thus, since no typical lithium compound has a binding energy of about 54 eV and since there is no clear evidence indicating that the low binding energy shoulder should be composed of two peaks, this shoulder was fit with only one peak as shown in Fig. 10. Therefore, we assign this low binding energy peak to a metallic Li and attribute the width of the peak to inhomogeneous broadening, matrix effects, or surface states [21]; an abundance of surface states may result from the highly dispersed and amorphous nature of the black electrodeposit. As discussed later, the potential used to form the black electrodeposit is too positive to produce elemental Li; therefore, we believe the metallic Li is actually present as a Li–Al alloy (*vide infra*).

Figure 11 shows the high resolution spectrum for the Al 2*p* region. In this figure, the major peak has a binding energy of 73.4 eV. In addition, there is a small low binding energy peak at 70.5 eV. The data could be fit quite well using just these two peaks; however, a binding energy of 73.4 eV does not correspond to any aluminium compounds that are likely to be present in this film. Fitting the major feature with two peaks, as shown in Fig. 11, gives two binding energies of 74.0 and 72.5 eV. These binding energies correspond reasonably well with the accepted values for alumina (74.2 ± 0.5 eV) and elemental Al (72.8 ± 0.2 eV) [17, 22]. The value for the alumina peak is on the high side of median, indicating a γ-type alumina phase; although, as discussed earlier, XRD analysis indicates the presence of a perovskite-type alumina phase. We tentatively assign the peak at 72.5 eV to a metallic Al. Its binding energy is slightly lower than that for elemental Al, but this could be due to surface states, as discussed above for the metallic Li. The small low binding energy peak at 70.4 eV does not correspond to any normal aluminium compounds since it has a binding energy much lower than that of elemental Al. This indicates that the aluminium is in a chemically reduced electronic state. Thus, a Li–Al alloy may be formed in which Li is responsible for generating a δ–charge on the Al, thereby shifting the peak to a binding energy lower than that of Al^0. Therefore, we tentatively assign the peak at 72.5 eV to a metallic $Al^{\delta-}$ in a Li–Al alloy. The metallic Al at 72.5 eV may be elemental Al, or it may be another Li–Al alloy with a lower lithium content.

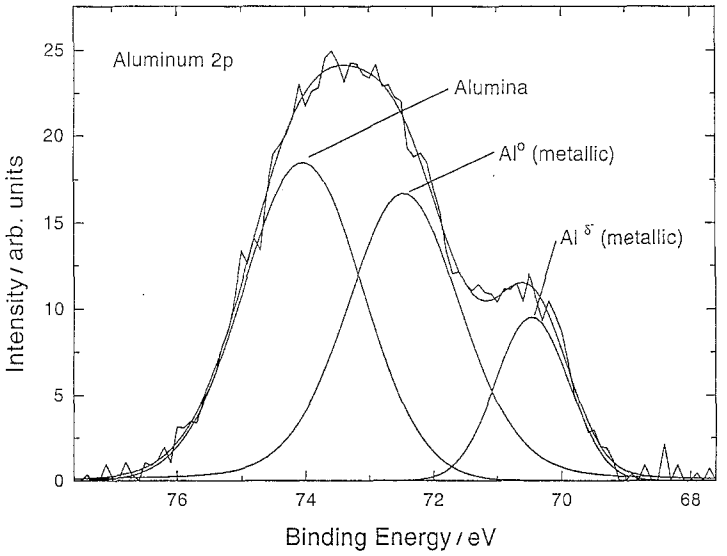

Fig. 11. High resolution XPS spectrum of Al 2*p* region for the sample shown in Fig. 9.

Table 4. Summary of high resolution XPS analysis

Element/ transition	*Peak energy* /eV	*FWHM* /eV	*Concentration* /at %	*Tentative peak assignments*
Cl $2p_{3/2}$	198.4	1.4	27	Cl^- (LiCl)
Li 1*s*	55.9	1.2	21	Li^+ (LiCl)
Li 1*s*	54.7	2.2	7	Li^0 (Li-Al alloy)
Al 2*p*	74.0	2.2	4.5	Al^{3+} (Al_2O_3)
Al 2*p*	72.5	2.1	4.5	Al^0 (elemental Al)*
Al 2*p*	70.4	1.3	1.5	$Al^{\delta-}$ (Li–Al alloy)
O 1*s*	530.6	3.1	19.5	O^{2-} (Al–O, Li–O)
N 1*s*	400.0	5.0	2	melt cation
C 1*s*	284.8	5.8	16	melt and other carbon materials

* This may also be metallic Al in a Li–Al alloy.

In addition to the high resolution lithium and aluminium spectra, high resolution spectra were also acquired for Cl and O spectral regions. The Cl 2*p* spectrum is almost a perfect spectrum for LiCl with a peak binding energy of 198.4 eV for the $2p_{3/2}$ transition. The O 1*s* spectrum, on the other hand, was a broad mixture of overlapping oxide states. The peak binding energy of 530.6 eV indicates that the main component is an alumina. The analyses of the high resolution Cl 2*p* and O 1*s* spectra, along with results from the high resolution spectra of the Li 1*s* and Al 2*p* regions, are shown in Table 4.

In summary, the XPS results indicate that the film is composed of approximately 50% LiCl, 20% carbonaceous material, 13% of metallic phases containing lithium and aluminium, 11% alumina, and 6% of other oxides and hydroxides. The presence of LiCl and an alumina phase are confirmed by the XRD results; however, no diffraction lines could be found for the metallic phases. Caution should be applied when using the metallic Li and Al results to estimate any Li–Al alloy compositions because lithium is well-known to preferentially segregate to the surface of Li–Al alloys [23]. Although ion sputtering can remove the top lithium-rich layer in the case of flat alloy samples, this is not the case for small alloy particles, where sputtering will only expose more isolated particles having a lithium-enriched surface. Therefore, for small alloy particles, the measured lithium content will depend on the particle size, the XPS excitation energy, and the degree of surface segregation [24].

The XPS analyses of two additional black electrodeposits prepared at −1.4 V showed only small amounts of the metallic phases in one sample and no metallic phases in the other sample; instead, the spectra were dominated by the peaks for LiCl and alumina. Therefore, although all electrodeposits are black and visually appear to contain metallic components, the metallic phases are difficult to observe with surface techniques such as XPS. It is likely that the precipitated LiCl, formed during electrodeposition of the Al metallic phases (Equation 1), coats the metallic particles. Ion sputter will only expose more particles which are still coated with LiCl.

3.5. *Electrochemistry of the black electrodeposit on Ni foil electrodes*

During preparation of samples for XRD and XPS analyses, it was noticed that the initial open-circuit potentials of the black electrodeposits on nickel were at much more negative potentials than the stripping potential found at GC. Also, the electrodeposit that contained a significant amount of the metallic phases had an initial open-circuit potential of −0.90 V, whereas, other samples with little or no detectable metallic phases displayed more positive open-circuit potentials. Therefore, we decided to investigate further the open-circuit and slow anodization behaviours of the black electrodeposit at nickel foil electrodes.

After charging an 8 cm^2 nickel foil electrode at −1.4 V for 22 h in a LiCl buffered neutral melt, the initial open-circuit potential of the electrodeposit was −1.18 V. The open-circuit potential was monitored for about 40 min, and then a constant current of 25 $\mu A\,cm^{-2}$ was imposed for about 5 min. The electrodeposit was returned to open-circuit for about 5 min before imposing the 25 $\mu A\,cm^{-2}$ current again. The potential trace of this experiment is shown in Fig. 12. At open-circuit the potential drifts slowly to more positive potentials, until at about 2250 s, the applied current causes a rapid jump to positive potentials. Importantly, the potential returns to more negative potentials when the electrodeposit is returned to open-circuit at about 2600 s. This behaviour is

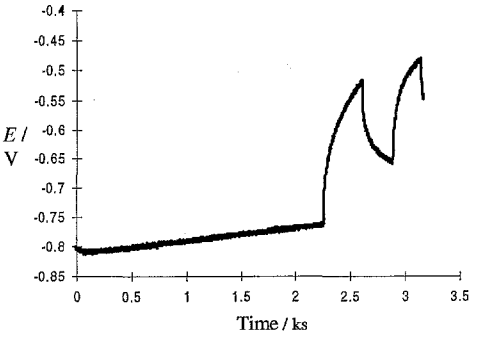

Fig. 12. Chronopotentiometric experiment showing open-circuit and oxidation behaviour (25 $\mu A\,cm^{-2}$) of a black electrodeposit prepared on Ni foil at −1.4 V in 1.1 : 1.0 : 0.1 $AlCl_3$: EMIC : LiCl.

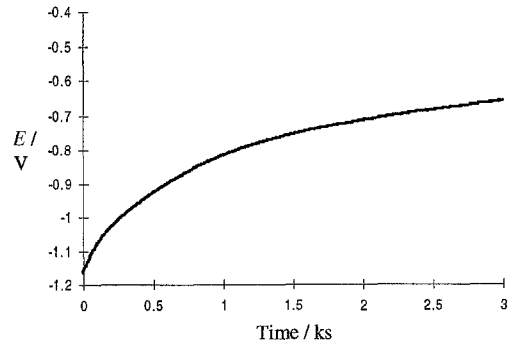

Fig. 13. Chronopotentiometry for oxidation ($0.5\,\mu A\,cm^{-2}$) of a black electrodeposit prepared on Ni foil at -1.4 V in 1.1 : 1.0 : 0.1 $AlCl_3$EMIC : LiCl.

repeated when the second current transient is applied. These results are significant because they indicate that small amounts of charge can be recovered from the electrodeposit at potentials more negative than -0.3 V, when nongraphitic electrodes are used. This is reinforced by the chronopotentiogram in Fig. 13, where an electrodeposit prepared at -1.4 V for 10 h on a $2\,cm^2$ Ni foil is oxidized for 50 min at $0.5\,\mu A\,cm^{-2}$; the potential slowly increases from -1.17 to -0.65 V during this experiment. It should be noted, however, that in our studies only porous graphite rods have shown any substantial charge recover at the more negative potentials (Fig. 4(a) and 4(b)); charge recovery at nongraphitic electrodes is extremely low.

4. Discussion

4.1. *Nature of metallic phases electrodeposited from LiCl buffered neutral melts*

As discussed above, only the LiCl buffered neutral melt allowed isolation of a black electrodeposit for analysis. This material contains LiCl, metallic phases, and aluminas, where the aluminas are most likely produced from reaction with water or oxygen during sample transfer. Analysis of the metallic phases shows the presence of 7 at % Li and 6 at % total Al; however, this lithium analysis may be much higher than the true bulk composition due to surface segregation of Li. Therefore, we can only speculate that the metallic Li and Al phases are produced by co-reduction of Li^+ and $AlCl_4^-$ from the LiCl buffered neutral melt. Reduction of $AlCl_4^-$ will produce large quantities of LiCl through Equation 1. The potential for this reduction (~ -1.4 V) is near the thermodynamic potential expected for $AlCl_4^-$ reduction in a basic, chloride-rich $AlCl_3$–EMIC molten salt [25]; however, no metallic aluminium has ever been electrodeposited from unbuffered neutral or basic melts (i.e., melts not containing alkali metals) due to the high kinetic stability of $AlCl_4^-$ [25]. Metallic Al can only be electrodeposited from acidic, $AlCl_3$-rich melts containing the $Al_2Cl_7^-$ ion [2].

It is important to note that the deposition potential for the black electrodeposit, which begins at about -1 V (see Figs 4 and 5), is approximately 1.0 V positive of the potential for elemental Li electrodeposition at -2.02 V in a 1.1 : 1.0 : 0.1 $AlCl_3$: EMIC : LiCl melt [26]. Therefore, the metallic Li is not likely to be elemental Li; instead it is probably present as a Li-Al alloy.

The common Li–Al alloys are α-Li_xAl and β-LiAl, where α-Li_xAl is a solid solution of Li in f.c.c. Al with a maximum solubility of $\sim$1 at % Li at room temperature [28], and β-LiAl is a congruently melting alloy having a b.c.c. structure and a narrow room-temperature composition range centred at 50 at % Li [28]. The potential of the $(\alpha + \beta)$ Li–Al biphasic region is about 0.45 V positive of the potential for elemental Li at 300 K [27], which places it at -1.6 V against the Al/Al(III) reference potential used in this study. Therefore, the potential for the black electrodeposit is approximately 0.55 V positive of the potential for the $(\alpha + \beta)$ Li–Al alloy phase region, and it is unlikely that the black electrodeposit contains this biphasic region. Also, if the $(\alpha + \beta)$ phase field were formed, it would maintain a constant potential of -1.6 V for Li–Al alloys having compositions from 1 to 50 at % Li; this is certainly not observed for the black electrodeposit.

A metastable α' phase also exists in the Li–Al alloy system; this phase has an ordered $AuCu_3$-type ($L1_2$ superlattice) structure [28]. The $(\alpha + \alpha')$ Li–Al phase field ranges in composition from 5.0 to 24.4 at % Li at 20 °C [28]. Although we do not have electrochemical information on this phase field, it is likely to have a potential intermediate between elemental Al at 0 V and the $(\alpha + \beta)$ phase field at -1.6 V. Therefore, we postulate that the metallic Li found in the black electrodeposit may be contained in the $(\alpha + \alpha')$ metastable Li–Al phase field. However, because of the lack of XRD information on these metallic phases, we can not rule out the possibility that the Li is contained in some other metastable amorphous Li–Al alloy phase. It is important to re-emphasize that the deposition potentials seen in our experiments, preclude the possibility that the β-LiAl phase is formed in these melt systems, as claimed by Fung and Chau [7].

The two metallic Al phases identified in the Al 2*p* XPS spectrum may be two Li–Al alloys (perhaps α and α'), or they may be a mixture of elemental Al and of alloyed Al in the $(\alpha + \alpha')$ Li–Al phase region. Elemental Al may be produced by electrochemical reduction of $AlCl_4^-$ through Equation 1, or it may be formed by chemical reaction of an initially electrodeposited Li–Al alloy with $AlCl_4^-$. This later explanation is consistent with the gradual positive shift in potential seen for the black electrodeposits as it remains in contact with the molten salt electrolyte (Figs 12 and 13). It is also possible the electrodeposition process is a mixture of elemental Al deposition and codeposition of Li–Al alloys. Again, the lack of XRD data on the Al metallic phases makes conclusive structural assignments impossible. What is important, however, is the observation of metallic Al phases which supports the presence of a metal or alloy electrodeposition process (e.g., via Equation 1).

4.2. *Comparison of electrochemistry in LiCl, NaCl and KCl buffered neutral melts*

As shown earlier (Figs 4 and 6), the electrochemical process starting at −1.0 V is most pronounced for the LiCl buffered neutral melt and decreases in the order LiCl > NaCl > KCl. Because we now believe this process involves, at least in part, the reduction of $AlCl_4^-$ to elemental Al or an Al alloy, the observed trend can be explained by well-known chemistry describing the thermal stability of oxyanion-containing molten salts. For molten salts containing complex oxyanions (e.g., NO_3^-, SO_4^{2-}, and CO_3^{2-}), the thermodynamic stability is directly proportional to $r^{1/2}/Z$, where r and Z are the ionic radius and charge, respectively, of the melt cation [29]. Therefore, the thermodynamic stability of the oxyanion increases as the cation radius for constant Z, and so the thermal stabilities of alkali metal oxyanion molten salts increase in the order $Li^+ < Na^+ < K^+$ (e.g., $LiNO_3 < NaNO_3 < KNO_3$) [29]. This thermodynamic trend is also reflected in the kinetic stability of these molten salts, as expected from linear free-energy correlations [30]. The kinetic trend can also be rationalized from differences in the polarizing strengths of the alkali metals which decrease in the order $Li^+ > Na^+ > K^+$. From this trend, Li^+ is expected to polarize and destabilize the oxyanion most.

The same principles described above for oxyanion molten salts clearly apply to the $AlCl_4^-$ anion in buffered neutral melts. In fact, Fung and Chau [31] have demonstrated with NMR techniques that Li^+ ions do polarize the $AlCl_4^-$ anion in LiCl buffered neutral melts. In addition, Boon *et al.* [32] have structurally characterized the compound $(Na)(EMI)(AlCl_4)_2$ in which the Na^+ cations are seen to preferentially interact and distort the $AlCl_4^-$ anions; the EMI^+ cations do not interact with the $AlCl_4^-$ anions in this structure [32]. Therefore, the distortion and instability of $AlCl_4^-$ is expected to increase in the order $EMI^+ \leqslant K^+ < Na^+ < Li^+$. Because the reduction in Equation 1 is essentially a decomposition of the $AlCl_4^-$ anion, its kinetically limited reduction is expected to be highest for buffered neutral melts containing Li^+ and lowest for the unbuffered 1:1 $AlCl_3$:EMIC molten salt; this is exactly what is observed.

An interesting test of the above reasoning is to see if gradual addition of Li^+ will increase the currents seen in the −1 to −1.6 V range. We have performed this test at a graphite rod electrode in a qualitative manner. Aluminum chloride was incrementally added to a 1:1 $AlCl_3$:EMIC melt containing a large excess of solid LiCl, dissolving portions of the LiCl through the buffering reaction and producing neutral buffered melts containing Li^+ concentrations from 0 to 150 mM. The melt temperature was maintained at 29 °C for these experiments using an aluminium heating block. The melts were stirred for several hours to ensure complete reaction of $AlCl_3$ with LiCl. In the 1:1 unbuffered melt, no currents were seen in the −1 to −1.6 V potential range at a graphite rod electrode, except for those associated with the intercalation process starting at −1.6 V. As $AlCl_3$ was added to the melt/LiCl mixture, reduction currents became obvious in the −1 to −1.6 V potential range, and the anodization waves found in Fig. 4(a) also appeared. These results are consistent with Li^+ promoting the decomposition of the $AlCl_4^-$ anion, and they also confirm that the electrodeposition process from −1 to −1.6 V is not due to incomplete buffering as postulated for the NaCl buffered neutral melts [5].

We have also noted that raising the temperature of a LiCl buffered neutral melt (75 mM Li^+) in 20 °C increments from 30 to 90 °C, increases both the cathodic current at −1.4 V and the area of the stripping wave at about −0.3 V (i.e. the rate of deposition of the black electrodeposit is increased). This observation is consistent with a kinetically controlled process and is contrary to an 'incomplete buffering' explanation for the electrodeposition. If complete buffering were a problem, the elevated temperature should increase the rate of the buffering reaction and cause a *decrease* in the −1.4 V deposition and −0.3 V stripping currents.

Given that reduction of the LiCl buffered neutral melt at the appropriate potential appears to produce elemental Al and a Li–Al alloy phase, or two Li–Al alloys, the question remains as to the nature of the nonintercalating reduction processes seen in the NaCl buffered neutral melt. The similar electrochemistry of the two melts at graphitic electrodes (Figs 4 and 6) supports the hypothesis that elemental Al and/or Na–Al alloys are formed in the NaCl buffered neutral melt. The nature of any Na–Al alloys is open to debate, however, because Na does not alloy with Al as easily as does Li [33]. The slow rate of electrodeposition in the NaCl system has hampered our ability to make quantifiable samples from this melt.

4.3. *Nonintercalating electrochemistry as graphite rods versus graphite sheets*

The higher cycling efficiencies for the nonintercalating process seen at the graphite rod (100%, Fig. 4) versus the graphite sheet (50–60%, Fig. 6) for both LiCl and NaCl buffered neutral melts can be understood from the higher surface area of the porous graphite rod. The high surface area leads to a higher dispersion of the metallic electrodeposit which maintains better physical contact with the substrate electrode and helps avoid passivation by the precipitated LiCl or NaCl. Also, the porous nature of the graphite rod may help protect the metallic deposit from continued reaction with the melt, making it possible to observe the more negative oxidation wave which is not seen at the graphite sheet electrode. The pores may also maintain a segregated high chloride activity at the electrodeposit which can lead to more negative Al stripping potentials, as in the case of basic $AlCl_3$–EMIC molten salts [25]. Finally, it is possible that some intercalation reactions occur that help stabilize the black electrodeposit since cycling efficiencies are high only for the

two graphitic electrodes, while efficiencies are extremely poor at nonintercalating electrodes.

If the black electrodeposit formed in the LiCl melt is to be used as a rechargeable anode, these results suggest that the substrate electrode should be porous, have a high surface area, and be graphitic in nature (e.g., petroleum coke). Fung and Chau demonstrated cycling efficiencies from 40 to 90% for the Li–Al/Al electrodeposit at aluminium substrate electrodes; however, their deposition-stripping times were limited to only about 1 min, where passivation by LiCl may not be too severe [7]. Using porous graphite rod substrates, we have demonstrated high cycling efficiencies for long charge–discharge cycles, both here and in a previous publication [11].

5. Conclusions

In this paper we have presented a number of experimental observations regarding the electrochemistry of unbuffered and buffered neutral $AlCl_3$–EMIC room-temperature molten salts. The results of these studies have practical consequences on the applicability of these melts as battery electrolytes and as electrochemical solvents in general:

(i) Unbuffered 1:1 $AlCl_3$:EMIC functions as a DIME cell electrolyte; however, the instability of the EMI^+ cation in the graphite lattice appears to preclude its use in a rechargeable graphite intercalation anode.

(ii) The LiCl buffered neutral melt is reduced between −1 to −1.6 V to produce a partially insulating film composed of LiCl and at least two metallic phases. The metallic phases are tentatively assigned as elemental Al and a Li–Al alloy phase, or two Li–Al alloy phases. The formation of this film may interfere with any electrochemistry (particularly low current density processes) occurring negative of −1 V in these melts and may eventually block the surface of graphitic and nongraphitic electrodes. Therefore, it is unlikely the LiCl buffered neutral melts can be employed as electrolytes for graphite intercalation anodes. Although the film itself can function as a rechargeable anode, its cycling efficiency is poor except in the case of porous graphite electrodes. Also, the voltage difference between deposition and stripping of this film is approximately 1 V, and so, significant energy losses will occur if this film is used as a rechargeable anode.

(iii) The NaCl buffered neutral melt displays electrochemistry at graphite electrodes similar to the LiCl system, indicating the formation of a film similar to that discussed in (ii) above. However, we have not been able to characterize the film produced in the NaCl buffered neutral melt, and Na is not expected to alloy with Al as easily as Li. Again, such film formation is expected to limit the usefulness of this melt as an electrolyte for graphite intercalation anodes, and the film itself is impractical as a rechargeable anode, except possibly at porous graphite electrodes.

(iv) The KCl buffered neutral melt does not exhibit the nonintercalating reduction processes seen in the LiCl and NaCl systems. Therefore, we postulate that a KCl-metallic film does not form in the KCl buffered neutral melt, or it forms too slowly to be observed by the experimental methods used in these investigations.

(v) The rate of electrochemical reduction of the $AlCl_4^-$ anion in the MCl buffered neutral melts increases in the order KCl < NaCl < LiCl. This trend is explained by the decreasing thermodynamic and kinetic stability of the $AlCl_4^-$ anion caused by the decreasing $r^{1/2}/Z$ ratio of the alkali metal cations in this series.

Acknowledgements

This work was support by the Air Force Office of Scientific Research through funding to the Frank J. Seiler Research Laboratory.

References

[1] R. T. Carlin, H. C. De Long, J. Fuller and P. C. Trulove, *J. Electrochem. Soc.* **141** (1994) L73.
[2] C. L. Hussey, *in* 'Chemistry of Nonaqueous Solvents' (edited by A. Popov and G. Mamantov), VCH, New York (1994), chapter 4.
[3] R. T. Carlin and J. S. Wilkes, *in* 'Chemistry of Nonaqueous Solvents' (edited by A. Popov and G. Mamantov), VCH, New York (1994), chapter 5.
[4] C. Scordilis, J. Fuller, R. T. Carlin and J. S. Wilkes, *J. Electrochem. Soc.* **139** (1992) 694.
[5] T. L. Riechel and J. S. Wilkes, *ibid.* **140** (1993) 3104.
[6] I. C. Quarmby, R. A. Mantz, L. M. Goldberg and R. A. Osteryoung, *Anal. Chem.* **66** (1994) 3558.
[7] Y. S. Fung and S. M. Chau, *J. Appl. Electrochem.* **23** (1993) 346.
[8] J. L. Wong and J. H. Keck, Jr., *J. Org. Chem.* **39** (1974) 2398.
[9] J. O. Besenhard, H. Möhwald and J. J. Nickl, *Carbon* **18** (1980) 339.
[10] Z. Zhang and M. M. Lerner, *J. Electrochem. Soc.* **140** (1993) 742.
[11] R. T. Carlin, J. Fuller and M. Hedenskoog, *ibid.* **141** (1994) L21.
[12] K. Kinoshita, 'Carbon: Electrochemical and Physiochemical Properties', J. Wiley & Sons, New York (1988).
[13] M. M. Doeff, Y. Ma, S. J. Visco and L. C. De Jonghe, *J. Electrochem. Soc.* **140** (1993) L169.
[14] N. Bartlett and B. W. McQuillan, *in* 'Intercalation Chemistry' (edited by M. S. Whittingham and M. Stanley), Academic Press, New York (1982), chapter 2.
[15] JCPDS card 42-423.
[16] N. N. Greenwood and A. Earnshaw, 'Chemistry of the Elements', Pergamon Press, New York (1984).
[17] J. F. Moulder, W. F. Stickle, P. E. Sobel and K. D. Bomben, 'Handbook of Photoelectron Spectroscopy', Perkin–Elmer Corporation, Physical Electronics Division, Eden Prairie, MN (1992).
[18] J. P. Contour, A. Salesse, M. Froment, M. Garreau, J. Thevenin and D. J. Warrin, *J. Microsc. Spectrosc. Electron.* **4** (1979) 483.3.
[19] C. D. Wagner, *in* 'Practical Surface Analysis', 2nd edn, vol. 1, 'Auger and X-Ray Photoelectron Spectroscopy' (edited by D. Briggs and M. P. Seah), J. Wiley, Chichester (1985, appendix 5.
[20] K. Kanamura, H. Tamura and Z. Takehara, *J. Electroanal. Chem.* **333** (1992) 127.
[21] W. F. Egelhoff, *Surf. Sci. Rept.* **6** (1987) 253.
[22] C. D. Wagner, D. E. Passoja, H. F. Hillary, T. G. Kinsky, H. A. Six, W. T. Jansen and J. A. Taylor, *J. Vac. Sci. Technol.* **21** (1982) 933.
[23] H. Ebel, M. F. Ebel, R. Svagera and Winklmayer, *J. Electron Spectrosc. Relat. Phenom.* **57** (1991) 15.

[24] T. J. Carney, P. Tsakiropoulos, J. F. Watts and J. E. Castle, *Int. J. Rapid Solidification* **1990** (1990) 189.
[25] R. T. Carlin and R. A. Osteryoung, *J. Electrochem. Soc.* **136** (1989) 1409.
[26] C. Scordilis-Kelley and R. T. Carlin, *ibid.* **140** (1993) 1607.
[27] J. N. Reimers and J. R. Dahn, *Phys. Rev. B.* **47** (1993) 2995.
[28] A. J. McAlister, *Bull. Alloy Phase Diagrams* **3** (1982) 177.
[29] K. H. Stern, *J. Chem. Ed.* **46** (1969) 645.
[30] J. H. Espenson, 'Chemical Kinetics and Reaction Mechanisms', McGraw-Hill, New York (1981).
[31] Y. S. Fung and S. M. Chau, *Inorg. Chem.* **34** (1995) 2371.
[32] J. A. Boon, R. T. Carlin, A. M. Elias and J. S. Wilkes. *J. Chem. Cryst.* **25** (1995) 57.
[33] A. J. McAlister, *Bull. Alloy Phase Diagrams* **4** (1983) 407.